Revealing Atomic-Scale Ionic Stability and Transport around Grain Boundaries of Garnet Li7La3Zr2O12 Solid Electrolyte

Bo Gao (✉ GAO.Bo@nims.go.jp)

National Institute for Materials Science (NIMS)   https://orcid.org/0000-0003-1183-656X

Randy Jalem

National Institute for Materials Science   https://orcid.org/0000-0001-9505-771X

Hong-Kang Tian

National Institute for Materials Science (NIMS)

Yoshitaka Tateyama

National Institute for Materials Science (NIMS)   https://orcid.org/0000-0002-5532-6134

Article

Revealing Atomic-Scale Ionic Stability and Transport around Grain Boundaries of Garnet $Li_7La_3Zr_2O_{12}$ Solid Electrolyte

Abstract

For real application to the all-solid-state batteries, understanding and control of the grain boundaries (GBs) are essential. However, the in-depth insight into the atomic-scale defect stabilities and transports of ions around the GBs is still far from understood. Here, the first-principles investigation on the promising garnet $Li_7La_3Zr_2O_{12}$ solid electrolyte GBs has been carried out. Our study reveals a GB-dependent behavior for the Li-ion transport correlated to the diffusion network. Especially, the $\Sigma 3(112)$ tilt GB model exhibits a quite high Li-ion conductivity comparable to that in bulk, and a fast intergranular diffusion contrary to the former concepts. Moreover, the preference of the electron accumulation at the $\Sigma 3(112)$ GB was uncovered in terms of the lower Li interstitial formation energies. This phenomenon is further enhanced by the presence of the Schottky-like defect, leading to the increase in the electronic conductivity at GBs, which plays a key role in the Li dendrite growth.

Introduction

Li-ion battery as an important energy storage device has been extensively applied to many fields, such as portable devices and electric vehicles.[1,2] Due to the existence of weakness of the organic liquid electrolyte in the traditional Li-ion battery (e.g. flammable), all-solid-state battery (ASSB) containing an inorganic solid electrolyte is one of the most promising candidates of the next-generation battery owing to its improved safety and cycle stability.[3–5] Through the long-term development, a variety of high-performance solid electrolytes (SEs) has been successfully synthesized, whose ion conductivities are comparable with the traditional liquid electrolytes.[6–9] Among of them, the garnet-type $Li_7La_3Zr_2O_{12}$ (LLZO) as a superior solid electrolyte has attracted great interest,[8,10,11] thanks to its high conductivity (~ 10^{-4} S/cm), wide electrochemical window (~ 6 eV)[12]. More attractively, LLZO shows good compatibility with the ultimate anode material, Li metal, to achieve an ASSB with a significantly high energy density.[13–17]

As most of the synthesized LLZO SEs are polycrystalline, the grain boundary (GB) has an inevitable influence on their performances. However, until now, this underlying GB effect has not been thoroughly understood yet. For example, numerous works have reported the resistance at GB related to the decrease in the ion conductivity in LLZO,[18–21] while some other studies have observed contradictory results, where the sample with small grain size has higher conductivity than that containing large-sized grains, indicating the faster ion transport at the GBs.[22–24] Moreover, GBs are expected to contribute to the Li dendrite growth in LLZO,[25–27] which leads to the short-circuiting of the cell[22,28–31]. It is reported that the inhomogeneous depletion[30] and low ion conductivity[32] at the GB are responsible for the dendrite growth. Particularly, recent works have proposed that the dendrite propagation originates from the high electronic conductivity,[28,33] which is reported to be appeared at the GB[34].

Thoroughly unraveling these serious GB issues require a comprehensive understanding of the ion diffusion, defect chemistry, and electronic properties at GB. Especially, the Li-ion conductivity at the GB has been revealed using the classical simulation method, where the GB resistance is sensitive to the GB structure and temperature.[21] However, the in-depth atomistic mechanism of Li-ion transportation at GBs has not been established yet. First-principles simulation based on the atomistic model as a powerful way can provide comprehensive results about the properties of SE. Especially for LLZO, it has been extensively used to explain the phase transition[35], migration mechanism[36], electrochemical window[12], defect chemistry[37], and the phenomena on the surface and at the interface with Li metal[38,39]. Unfortunately, as far as

we know, there is no report of the study on these significant GB issues based on the first-principles simulation.

Herein, we have reported a study on the atomistic diffusion and defect chemistry of ions at the GBs of LLZO using the first-principles density functional theory (DFT), aiming to discover the GB effects on the ion conductivity and dendrite growth within LLZO SE. We have observed the distortion and decomposition of ZrO_6 unit at the GBs. It is revealed that Li^+ diffusivity is strongly dependent on the migration network determined by the GB atomistic structure. Especially, the $\Sigma3(112)$ GB model with the analogous migration network shows the comparable conductivity with that of bulk, whereas the $\Sigma1(110)$ GB model exhibits the significantly slow diffusivity. Moreover, through the calculated defect formation energies, the enrichment of Li interstitials at the GB has been observed, introducing the extra electron localized at the GB and leading to the enhanced electronic conductivity, which is a key in the dendrite growth. To the best of our knowledge, this study is the first work for simulating the GB in SE using first-principles method thus far. We believe that this work provides a novel perspective for elucidating the GB effect on the SE.
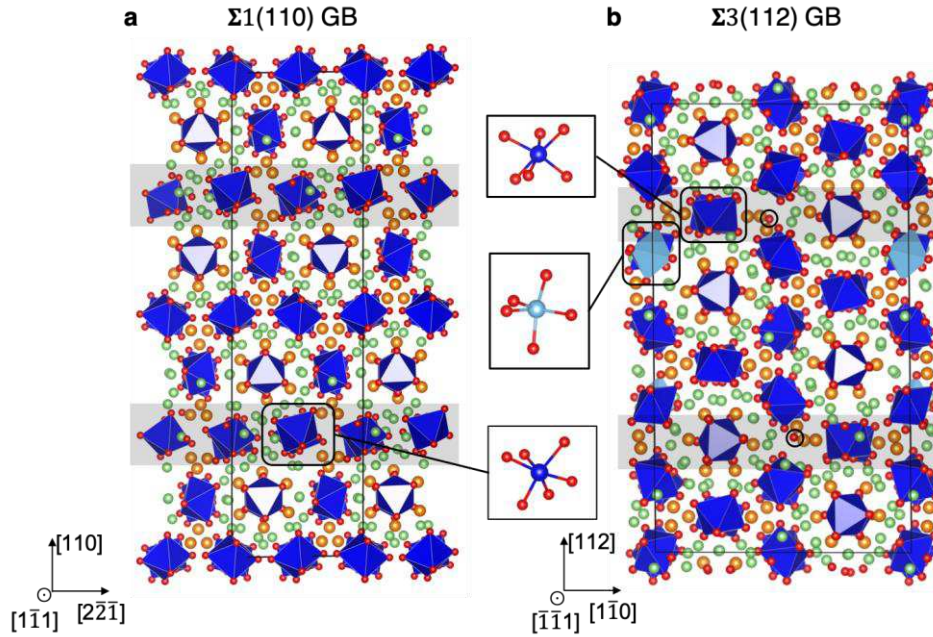
Figure 1 Energetically favorable structures of GB models of LLZO. (a) atomistic structure of Σ1(110) GB model, (b) atomistic structure of Σ3(112) GB models. The insets show the geometries of ZrO_6 and ZrO_5 units at GBs. The grey areas indicate the regions of GB. The green, orange, red and dark blue spheres represent the Li, La, O, and Zr atoms, respectively. The dark blue polyhedrons refer to the ZrO_6 units. Especially in the Σ3(112) GB model, the light blue spheres and polyhedrons represent the 5-coordinated Zr atoms and ZrO_5 polyhedrons, respectively, and the isolated O atoms are highlighted with the black circles.

Results and Discussion

GB stabilities and structures. Considering the high computational cost in the DFT calculations, the symmetric tilt GBs with low-order coincident site lattices, Σ1(110) and Σ3(112) GBs, have been adopted. These selected GBs are the low-energy GBs in the BCC metals[21,40] since Zr occupies the BCC-type sublattices in LLZO. Through the sampling strategies, the energetically favorable configurations of both GB models have been obtained. The calculated GB formation energy (γ) of the Σ1(110) GB model is 0.63 J/m^2. The Σ3(112) GB model exhibits a comparatively lower γ of 0.6 J/m^2, which is relatively consistent with the value evaluated from the classical simulations (0.54 J/m^2)[21], indicating higher stability of this GB and more proportion in the polycrystalline sample. Meanwhile, the calculated density relative to that of bulk for Σ1(110) GB (96.27%) is lower than that of Σ3(112) GB (97.21%). The geometrical structures of both GB models are depicted in Figure 1. It is found that the ZrO_6 octahedrons are distorted at both GBs. Interestingly, at the Σ3(112) GB, part of ZrO_6

octahedrons are decomposed to ZrO_5 and isolated O ions. The calculated partial densities of states (PDOSs) of two GB models (Figure S2) show that the band gaps of the $\Sigma1(110)$ and $\Sigma3(112)$ GB models are about 3.6 and 3.5 eV, respectively, which are slightly reduced compared to the value in bulk (4.0 eV).
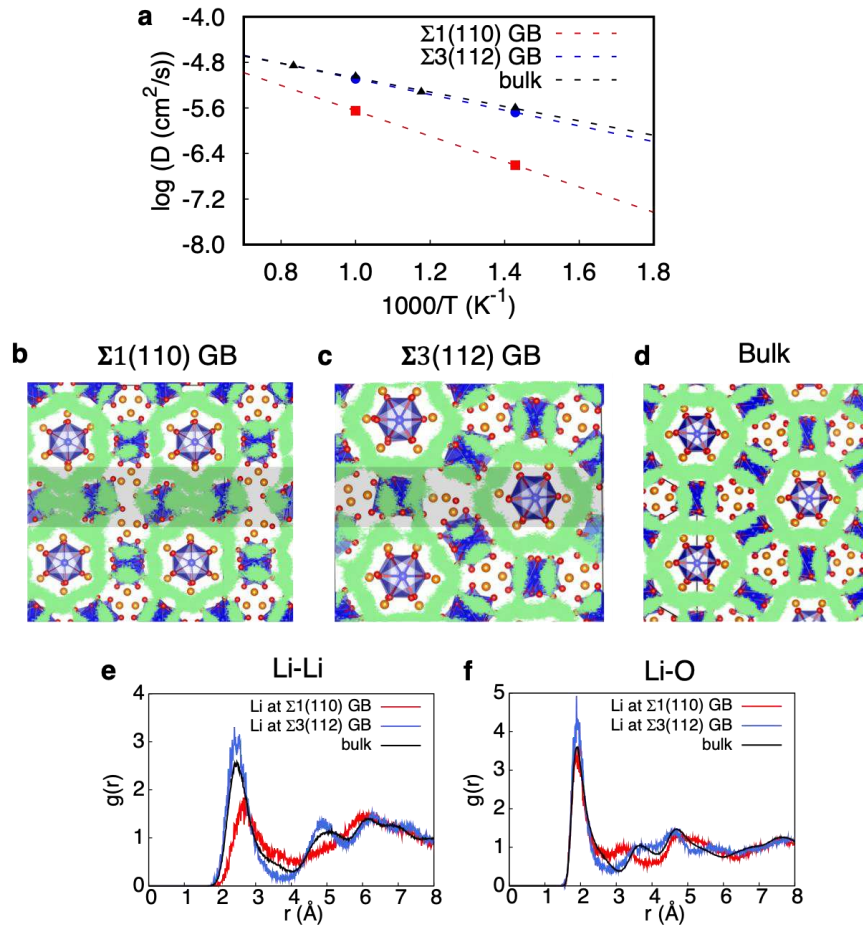

Figure 2 Results of FPMD simulations. (a) Arrhenius plots of diffusion coefficients in bulk, and $\Sigma1(110)$ and $\Sigma3(112)$ GB models of LLZO. (b-d) Li-ion trajectories accumulated from 0 to 35 ps in the MD simulations at 1000 K in the (b) $\Sigma1(110)$ and (c) $\Sigma3(112)$ GB models, and (d) bulk. The $\Sigma1(110)$ GB model is viewed along $[1\bar{1}1]$ direction, and $\Sigma3(112)$ GB model and bulk are viewed along $[\bar{1}\bar{1}1]$ direction. Considering the cubic-like symmetry of LLZO, the $[\bar{1}1\bar{1}]$ and $[\bar{1}\bar{1}1]$ directions can be regarded as the equivalent directions. (e-f) (e) Li-Li and (f) Li-O radial distribution functions averaged from 5 to 40 ps in the MD simulation at 1000 K of bulk, and the selected Li-ions at the $\Sigma1(110)$ and $\Sigma3(112)$ GBs of LLZO.

Table 1 Extrapolated Li-ion conductivities at the room temperature (298.15 K) (σ_{RT}) and activation energies (E_a) for bulk, and $\Sigma1(110)$ and $\Sigma3(112)$ GB models of LLZO.

	σ_{RT} (S/cm)	E_a (eV)
Bulk	1.43×10^{-3}	0.25
$\Sigma1(110)$	1.93×10^{-6}	0.44
$\Sigma3(112)$	7.17×10^{-4}	0.27

Ion transports at GBs. The first-principles molecular dynamic (FPMD) simulations have been performed to reveal the GB contribution to the Li-ion transportation in LLZO. The calculated Arrhenius plots of diffusion coefficients derived from the time-average mean square displacement (MSD) (Figure S3) are shown in Figure 2a. Intriguingly, we found that both investigated GB models show distinct diffusion behaviors. The diffusion coefficient of the $\Sigma3(112)$ GB model is obviously close to that of bulk, while $\Sigma1(110)$ GB model exhibits the remarkably slow diffusivity. The analogous GB-dependent nature of Li-ion diffusions has also been reported in the previous classical simulations.[21] The extrapolated conductivity at the room temperature (298.15 K) (σ_{RT}) based on the Nernst-Einstein equation and the calculated activation energies (E_a) are tabulated in Table 1. Note that the current calculated E_a of bulk (0.25 eV) is slightly lower than the experimentally measured value (0.30-0.35 eV)[8]. We attributed this to the adopted PBE functional in the DFT calculation, which overestimates lattice constant and underestimates the E_a. Nevertheless, the simulated result is well consistent with the previously calculated values (0.24-0.26 eV).[41,42] Accordingly, the calculated σ_{RT} (1.43×10^{-3} S/cm) is relatively higher than the values observed in experiments (4.6-5.2 $\times10^{-4}$ S/cm)[8]. The E_a of the $\Sigma3(112)$ GB model (0.27 eV) is slightly higher than that of bulk and the σ_{RT} (7.17×10^{-4} S/cm) is about half of that in bulk. In the contrast, the $\Sigma1(110)$ GB model shows a much higher E_a (0.44 eV) and a significantly lower σ_{RT} (1.93×10^{-6} S/cm) compared to those in $\Sigma3(112)$ GB model and bulk.

It is known that the Li-ion exhibits the 3-dimensional diffusion behavior in the LLZO.[36] Previous force field simulations have found that the Li-ion prefers to migrate with the GB plane in the SEs including the LLZO.[21,43] However, we have observed that the projected MSD (Figure S4a) across GB ([112] direction) for the atoms in the GB region is remarkably higher than those components within the GB plane ([$1\bar{1}0$] and [$11\bar{1}$] directions), indicating that the intergranular diffusion is relatively fast. It is noteworthy that these projected MSD results are governed by the selected size of the GB region. We then have calculated the projected MSDs averaged from

the whole atoms in the cells of $\Sigma 3(112)$ GB model and bulk. Although the total rate of diffusion across the GB in the $\Sigma 3(112)$ GB model is decreased (Figure S4b), it can still be comparable with the rates along the directions within the GB plane ([$1\bar{1}0$] and [$11\bar{1}$] directions), leading to a quasi-isotropic diffusion behavior. Furthermore, compared to that along the equivalent direction in the bulk (Figure S4c), the diffusion rate across the GB is apparently enhanced. These results prove the presence of a comparatively fast intergranular diffusion in the LLZO polycrystalline.

To understand the diffusion behaviors of GBs, the Li-ion trajectories accumulated from 0 to 35 ps in the MD simulations at the temperature of 1000 K have been depicted in Figure 2b-d. We found that the $\Sigma 3(112)$ GB model shows the analogous trajectories to those in bulk, while the trajectories in $\Sigma 1(110)$ GB model is obviously different from those in the bulk and $\Sigma 3(112)$ GB model. Especially for $\Sigma 3(112)$ GB, it is observed that there are several paths crossing the GB plane, which account for the fast intergranular diffusion.

The radial distribution functions (RDFs) have been calculated to understand the impact of the local atomic environment on Li$^+$ diffusion around GBs. The calculated RDFs averaged from the total atoms in the cells (Figure S5) show the almost same peak positions, indicating that the average densities of particles in bulk and two GB models are nearly identical. Therefore, the shift in peak position corresponds to the change of the interatomic distance between two ions. In the Li-Li RDFs (Figure 2e), the position of the first peak for the ions at the $\Sigma 3(112)$ GB is nearly identical to that in bulk, while it is up-shifted in the RDF of ions at the $\Sigma 1(110)$ GB, indicating a larger interatomic distance between two nearest Li-ions at the $\Sigma 1(110)$ GB. Moreover, in the Li-O RDFs (Figure 2f), although both GBs and bulks possess the nearly same positions for the first peak, the ions at the $\Sigma 1(110)$ GB shows the shift for the second peak. These distinct Li-ion atomic environments together with the different diffusion networks at the $\Sigma 1(110)$ GB are correlated to its atomistic structure, and responsible for its lower conductivity. Instead, the $\Sigma 3(112)$ GB with the similar atomic environments and diffusion trajectories to those of bulk shows better conductivity.

Unexpectedly, through the calculated MSD of O ions (Figure S6), we have observed the diffusions of O ions around the $\Sigma 3(112)$ GB at the elevated temperature. The selected snapshots in the MD simulation at the temperature of 1000 K (Figure S7) indicate that O ions can be migrated between neighboring Zr-O polyhedrons, leading to a diffusion of ZrO$_5$ unit (O vacancy-like diffusion) at the GB. These findings may account for the O vacancy diffusions observed in the isotope exchange experiments[44].
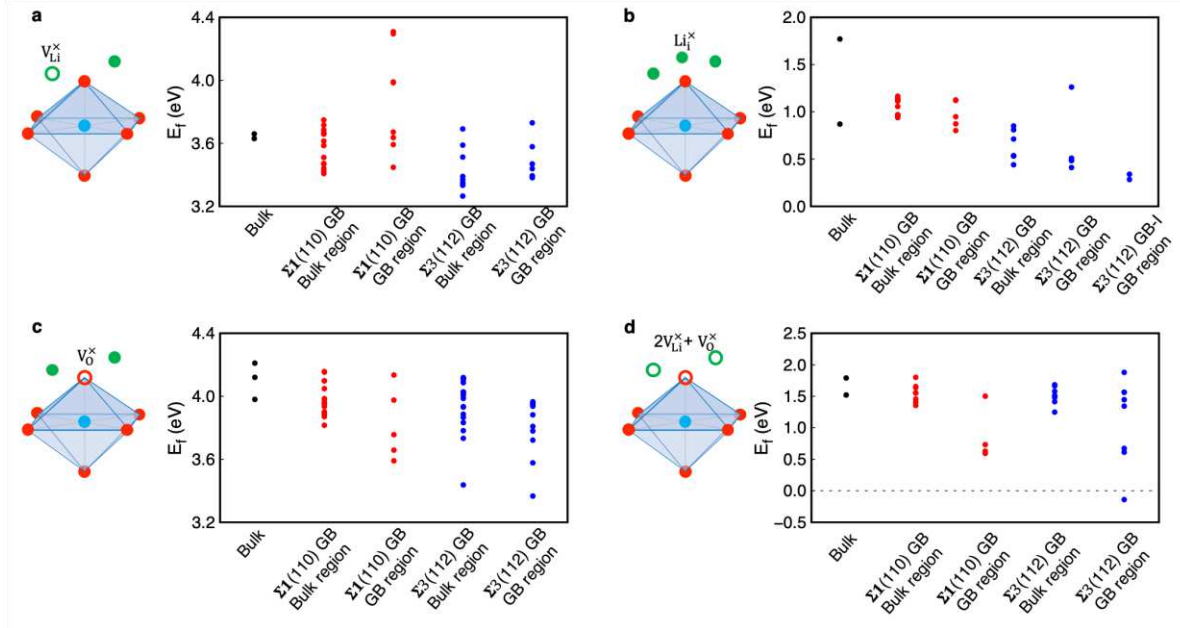
Figure 3 Calculated defect formation energies (E_f) for (a) $V_{Li}^{\times}$, (b) $Li_i^{\times}$, (c) $V_O^{\times}$, and (d) Schottky-like defect ($2V_{Li}^{\times}+V_O^{\times}$) in the bulk, and $\Sigma1(110)$ and $\Sigma3(112)$ GB models. The schematic illustrations of the configurations of these defects are shown in the left panels, where the hollow circles refer to the vacancies. The green, red and blue spheres represent Li, O, and Zr ions, respectively.

Ion stabilities at GBs revealed from defect chemistries. The intrinsic defects play an important role in determining the properties of LLZO, such as the electronic properties and dendrite growth.[37] Therefore, the defect chemistry at the $\Sigma1(110)$ and $\Sigma3(112)$ GBs of LLZO have been studied here. The predominant charge-neutral point defects in the LLZO bulk[37,45,46]: Li vacancy ($V_{Li}^{\times}$), Li interstitial ($Li_i^{\times}$), O vacancy ($V_O^{\times}$), and Schottky-like defect consisting of two Li vacancies and one O vacancy ($2V_{Li}^{\times}+V_O^{\times}$), have been considered in our work. As we mainly focus on the LLZO near the Li metal anode to understand the GB contribution to the dendrite growth, a typical reducing environment has been adopted in the calculation of defect formation energies (E_f), where LLZO is in equilibrium with Li and Li_2O. The calculated E_f values of bulk and both GB models have been plotted in Figure 3. Note that the high concentrations of charged defects and cation-antisite defects have been reported as well.[37] Those defect distributions around GBs will be investigated in future works.

The calculated E_f for $V_{Li}^{\times}$ at *24d* and *96h* sites in bulk are approximate to 3.6 eV (Figure 3a), which is in good agreement with the previously calculated values (3.54 eV).[46] Interestingly, we have found that there are several $V_{Li}^{\times}$ with significantly higher E_f at the $\Sigma1(110)$ GB, whose

maximum value (4.3 eV) is about 0.7 eV larger than that in bulk. These sites with remarkably high E_f will lead to the large barriers for Li^+ migrating from neighboring sites to these sites, which is one of the main reasons for the low Li^+ conductivity at this GB. Through analyzing the Li-Li coordination environments of the considered vacancies (Figure S8a), we found that, only for the sites at the GB with the elevated E_f, the coordination number within the cutoff radius of 2.7 Å is zero, indicating that these sites have the longer interatomic distances and the weaker electrostatic repulsion interactions with the neighbouring Li-ions. This is a potential origin of these high E_f. Compared to those at the $\Sigma1(110)$ GB, the $V_{Li}^{\times}$ at the $\Sigma3(112)$ GB shows the lower E_f owing to the closer Li-Li interatomic distances. Notably, part of sites in the $\Sigma3(112)$ GB model show the slightly decreased E_f. We attribute this to the reduced band gap, which raises the valance band maximum and the electrochemical potential of the electron, thereby increasing the chemical potential of Li, which is equivalent to the negative value of E_f of $V_{Li}^{\times}$, as discussed in recent studies.[47]

For $Li_i^{\times}$ in LLZO (Figure 3b), two sites located at *24d* and *48g* positions in bulk phase have been considered. The calculated E_f for $Li_i^{\times}$ at *48g* (0.87 eV) is much lower than that at the *24d* site (1.77 eV). The calculated Li-Li coordination numbers (Figure S8b) indicate that, under the cutoff distance of 2.2 Å, there is only one neighboring Li for $Li_i^{\times}$ at *48g*, in contrast to the three neighboring Li for $Li_i^{\times}$ at *24d*. This larger Li-Li interatomic distance of $Li_i^{\times}$ at *48g* induce the weaker electrostatic repulsion interaction, which is favorable for inserting the $Li_i^{\times}$. For the $\Sigma1(110)$ GB model, due to the small Li-Li coordination number (Figure S8b), the calculated E_f of $Li_i^{\times}$ (0.8 eV-1.13 eV) are close to the value at *48g* site in bulk. Intriguingly, in the $\Sigma3(112)$ GB model, we found that most of $Li_i^{\times}$ around the GB show the obviously lower E_f compared to those in the bulk and $\Sigma1(110)$ GB model. The lowest E_f is only 0.41 eV. Such low E_f is partially induced by the larger Li-Li interatomic distance, as indicated by the calculated Li coordination number (most of sites don't have the coordinated ions under the cutoff distance of 2.2 Å) (Figure S8b). Moreover, the electronic behaviors at the GBs may also have an influence on the E_f by varying the electrochemical potential of electron. The calculated partial densities of states (PDOSs) of both GB models with $Li_i^{\times}$ (Figure 4b,c) show the downshifts of the interstitial states compared with that of bulk (Figure 4a). Especially for $\Sigma3(112)$ GB, the interstitial states are decreased by approximately 0.4 eV from the conduction band minimum. These downshifts of the interstitial states may be correlated to the observed decrease of E_f of $Li_i^{\times}$ at the GB.

The charge densities associated with these interstitial states are shown in Figure 4. In the bulk and $\Sigma 1(110)$ GB models, the excess electrons from $Li_i^{\times}$ are localized around the La ions, similar to the finding in the simulation of the LLZO surface.[33,38] In stark contrast, the excess electrons are localized at the ZrO_5 pyramid at the $\Sigma 3(112)$ GB. The analogous phenomenon of this preferential reduction of the ZrO_5 unit has also been observed on the LLZO surface in contact with the Li metal.[39] Furthermore, we found that this electronic localization is independent of the position of $Li_i^{\times}$, as demonstrated by the additional partial charge density of the $\Sigma 3(112)$ GB model with a $Li_i^{\times}$ in the bulk region (Figure S9). These results imply that the $\Sigma 3(112)$ GB with the ZrO_5 pyramids shows the strong capability of capturing the extra electrons.
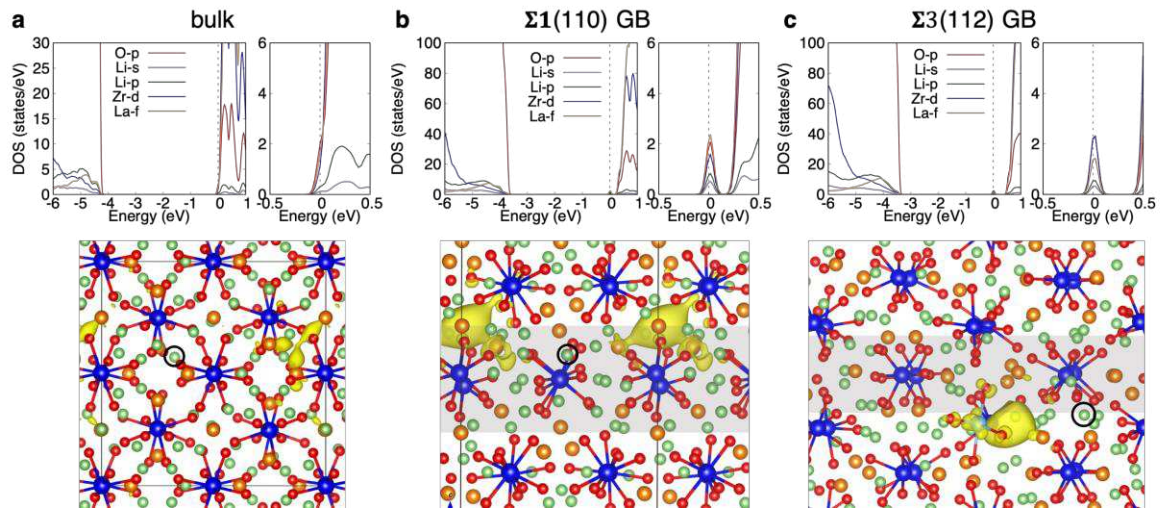

Figure 4 Calculated PDOSs (upper panel) and partial charge densities associated with the states in the energy range from -0.1 to 0.1 eV (lower panel) of (a) bulk with a $Li_i^{\times}$ at *48g*, (b) $\Sigma 1(110)$ GB model with a $Li_i^{\times}$ in the GB region, and (c) $\Sigma 3(112)$ GB model with a $Li_i^{\times}$ in the GB region. In the PDOSs, the dashed lines indicate the Fermi levels. The upper right panels refer to the enlarged PDOSs around the Fermi levels. For the partial charge densities, the isosurfaces are set to 0.005 $e/bohr^3$. The $Li_i^{\times}$ sites are highlighted using the black circles. The grey areas indicate the GB regions. The color scheme for atoms and polyhedrons is the same as Figure 1.

It is well known that the DFT calculation based on the PBE functional usually underestimates the band gap. Therefore, we have adopted the screened hybrid functional HSE06[48,49] to further examine our results. As it is difficult to perform the HSE06 calculations on the GB model with such a large cell due to the high computational cost, we have constructed two representative bulk models. The one contains a $Li_i^{\times}$ at *48g* Wyckoff position (Figure S10a),

and the other has a defect consisting of one $V_{Li}^{\times}$ and one $V_O^{\times}$ (Figure S10b), which equivalents to a Schottky-like defect combined with a $Li_i^{\times}$, in order to create a ZrO_5 pyramid in the cell. The calculated PDOSs show a pronounced increase in the band gap (over 5 eV). For the bulk with a $Li_i^{\times}$ (Figure S10a), the interstitial states are localized under the conduction band and dominated by the O-2p states. While in the bulk with $V_{Li}^{\times}+V_O^{\times}$ defect (Figure S10b), the interstitial states are apparently down-shifted, and mainly contributed by the Zr-4d and O-2p states from the ZrO_5 pyramid. These HSE06 calculations clearly prove the preference of electron localization at the ZrO_5 unit, which exists at the $\Sigma3(112)$ GB.

The calculated E_f of $V_O^{\times}$ (Figure 3c) in the bulk LLZO is from 3.9 to 4.3 eV. Besides, it is observed that parts of $V_O^{\times}$ at both GBs show the lower E_f than those in bulk. We consider that this is caused by the deformations and decompositions of ZrO_6 octahedrons at GBs.

For $2\,V_{Li}^{\times}+V_O^{\times}$ Schottky-like defect (Figure 3d), considering the strong electrostatic interactions between Li and O, the neighboring Li and O vacancies have been considered.[45] The calculated E_f for the representative defects in bulk is 1.5-1.8 eV. Similar to the $V_O^{\times}$, parts of defects at the $\Sigma1(110)$ and $\Sigma3(112)$ GBs show remarkably lower E_f values. Strikingly, we found that a studied Schottky-like defect containing the vacancy of isolated O ion (shown in the circle in Figure 1b) decomposed from the ZrO_6 octahedron at the $\Sigma3(112)$ GB shows the negative E_f (-0.14 eV), indicating that the model with this defect is energetically more stable. Therefore, we constructed a model with this Schottky-like defect, which is named as $\Sigma3(112)$ GB-I model, and further calculated the E_f for the $Li_i^{\times}$. Intriguingly, when we added two $Li_i^{\times}$ at the specific sites in the GB region, the interstitial formation energy (See Figure 3b) is further decreased to only 0.28 eV.

Mechanism of dendrite growth along GBs in LLZO/Li ASSB. Utilizing the calculated results of defect chemistries at the GBs, we herein make a discussion for the GB contribution to the dendrite growth in the LLZO/Li metal cell. In the region close to the Li metal anode (under the reducing environment), the LLZO bulk shows the lower E_f of $Li_i^{\times}$ compared to other defects, which is consistent with the previous study on the Al-doped LLZO.[45] This result implies the high concentration of $Li_i^{\times}$ and the tendency of Li enrichment in LLZO near the Li metal, which has already been found in the observation using EELS analysis.[50] Moreover, the calculated reduced E_f of $Li_i^{\times}$ in the GB region indicates the accumulation of Li at some specific GBs [e.g. $\Sigma3(112)$ GB], and the existence of the Schottky-like defects further decrease the E_f of $Li_i^{\times}$ thereby enhancing the enrichment of Li in the GB regions, which is expected to result

in the preferential deposition at GB during charging, which may be correlated to the recently reported crack formation in the LLZO.[51,52]

Furthermore, the excess electrons show a strong preference to be localized in the GB regions. These electrons, whose states are close to the conduction bands, would show the potentially high mobility, and high capability to combine with the excess Li ions to trigger the nucleation of Li^0 inside the SE.[33,34,53] Meanwhile, these excess electrons may lead to the redistribution of the electric field.[54] The GB with high electronic conductivity will facilitate the Li penetrations. All of these factors are critical for the dendrite propagation inside LLZO SE.

It is noteworthy that Li creep and plastic flow driven by the built-up pressure at the LLZO/Li interface during electrodeposition are also critical for the dendrite formation.[51,55,56] The current study focuses on the impact of the microstructure structure of GB, and provides a potential reason for the high electronic conductivity of LLZO, which has been widely reported as another major origin of the dendrite formation within SE.[17,33,34,53] Our study shows that the decomposition of ZrO_6 octahedron at the GBs plays an important role in the dendrite growth in LLZO. Specifically, the presence of the ZrO_5 pyramid decreases the E_f of $Li_i^\times$, and induces the electron localization, and the existence of the isolated O stabilizes the Schottky-like defect at the GB. It is interesting that this decomposition of ZrO_6 octahedron occurs at the energetically more favorable and denser $\Sigma3(112)$ GB instead of the less stable $\Sigma1(110)$ GB. These results imply that, in some situations, optimizing the microstructure of the GB, such as protecting the ZrO_6 polyhedron from degeneration, may be more significant than increasing the density and reducing the high-energy proportions of GB in the synthesis of the LLZO regarding the dendrite growth suppression.

In summary, we have utilized the first-principle method to systematically study the diffusions and defect stabilities of ions at the GBs of LLZO SE. The distortions and decompositions of ZrO_6 octahedra at GBs are revealed from the energetically favorable models. The results of MD simulations reveal the GB-dependent nature of Li-ion transportation. The $\Sigma3(112)$ GB shows a conductivity comparable to that of bulk due to the bulk-like Li^+ migration network, while $\Sigma1(110)$ GB with the distinct diffusion paths exhibits a significantly lower conductivity. Moreover, the higher Li vacancy formation energies at the $\Sigma1(110)$ GB induced from the larger Li-Li interatomic distance contributes to the low conductivity at the $\Sigma1(110)$ GB. The lower Li interstitial formation energies imply the Li accumulation at the $\Sigma3(112)$ GB, which is further enhanced by the presence of the Schottky-like defect. Furthermore, the ZrO_5

unit at the GB shows the propensity of capturing the excess electrons, resulting in the higher electronic conductivity, which is critical in the Li dendrite growth. Besides, the diffusion of O vacancy observed at the elevated temperature provides possible evidence for the O diffusion found experimentally. The current study provides a comprehensive knowledge of fundamental properties of LLZO GB, and a novel perspective in performance optimization of ASSBs.

Methods

GB structure construction. The GB models were constructed based on the Zr sublattice to preserve the ZrO_6 octahedron in the initial structure. To suppress the interaction between the neighbouring equivalent GBs, the distance between them are above 15 Å. All the Li sites are occupied in the initial GB models, and we performed a two-step procedure to search the energetically favorable Li distribution. First, we selected a series of different occupations of *24d* and *96h* sites in the GB models (Table S1) on the basis of the experimentally observed occupations (0.564 for *24d* site and 0.442 for *96h* site) . For each occupation, 10 structures were randomly constructed with the exclusion of the electrostatically unfavorable neighboring sites (distance between two Li-ions < 1.8 Å) and geometrically optimization is conducted (Figure S1a,b). The lowest-energy models of Σ1(110) and Σ3(112) GBs were adopted as input structures of subsequent molecular dynamic (MD) simulations. Second, 10 structures in the time range from 10 to 20 ps in the MD simulations at the temperature of 1000K have been sampled and subsequently geometrically optimized (Figure S1c,d). The lowest-energy models were used in the calculation of the electronic properties and defect formation energies of Σ1(110) and Σ3(112) GBs.

First-principles calculation. The DFT method was employed within the generalized gradient approximation of the Perdew, Burke, and Ernzernhof functional as implemented in the Vienna ab initio simulation package.[58] Electron−ion interactions were described using projector-augmented wave pseudopotentials[59], with the following valence electrons: $2s^1$ for Li, $2s^22p^4$ for O, $5s^24d^2$ for Zr, and $5s^25p^65d^16s^2$ for La. A plane-wave kinetic-energy cutoff of 520 eV and a k-spacing of 0.25 Å^{-1} in reciprocal space were used to achieve reliable results. First-principle molecular dynamic (FPMD) simulations were performed in the canonical (NVT) ensemble using the Nosé-Hoover thermostat[60] at 700 and 1000 K for bulk, Σ1(110) and Σ3(112) GB models, with a time step of 1 fs. Additional MD simulations at 850 and 1200 K were carried out for bulk. In the MD simulations, in order to trade off the computational cost and accuracy, the kinetic-energy cutoff and k-spacing were set to 450 eV and 0.5 Å^{-1} in reciprocal space,

respectively. The detailed methods for calculating the GB formation energy, time average mean squared displacement, and defect formation energy have been described in the supplementary information.

Competing interests

The authors declare no competing interests.

References

1. Boulineau, S., Courty, M., Tarascon, J.-M. & Viallet, V. Mechanochemical synthesis of Li-argyrodite Li_6PS_5X (X=Cl, Br, I) as sulfur-based solid electrolytes for all solid state batteries application. *Solid State Ion.* **221**, 1–5 (2012).

2. Goodenough, J. B. & Park, K.-S. The Li-Ion Rechargeable Battery: A Perspective. *J. Am. Chem. Soc.* **135**, 1167–1176 (2013).

3. Famprikis, T., Canepa, P., Dawson, J. A., Islam, M. S. & Masquelier, C. Fundamentals of inorganic solid-state electrolytes for batteries. *Nat. Mater.* **18**, 1278–1291 (2019).

4. Tian, Y. *et al.* Compatibility issues between electrodes and electrolytes in solid-state batteries. *Energy Environ. Sci.* **10**, 1150–1166 (2017).

5. Gao, B., Jalem, R., Ma, Y. & Tateyama, Y. Li^+ Transport Mechanism at the Heterogeneous Cathode/Solid Electrolyte Interface in an All-Solid-State Battery via the First-Principles Structure Prediction Scheme. *Chem. Mater.* **32**, 85–96 (2020).

6. Kamaya, N. *et al.* A lithium superionic conductor. *Nat. Mater.* **10**, 682–686 (2011).

7. Kato, Y. *et al.* High-power all-solid-state batteries using sulfide superionic conductors. *Nat. Energy* **1**, 16030 (2016).

8. Murugan, R., Thangadurai, V. & Weppner, W. Fast Lithium Ion Conduction in Garnet-Type $Li_7La_3Zr_2O_{12}$. *Angew. Chem. Int. Ed.* **46**, 7778–7781 (2007).

9. Liu, Z. *et al.* Anomalous High Ionic Conductivity of Nanoporous β-Li_3PS_4. *J. Am. Chem. Soc.* **135**, 975–978 (2013).

10. Duan, H. *et al.* Li/Garnet Interface Optimization: An Overview. *ACS Appl. Mater. Interfaces* **12**, 52271–52284 (2020).

11. Xu, L. *et al.* Garnet Solid Electrolyte for Advanced All-Solid-State Li Batteries. *Adv. Energy Mater.* **11**, 2000648 (2021).

12. Thompson, T. *et al.* Electrochemical Window of the Li-Ion Solid Electrolyte $Li_7La_3Zr_2O_{12}$. *ACS Energy Lett.* **2**, 462–468 (2017).

13. Krauskopf, T., Richter, F. H., Zeier, W. G. & Janek, J. Physicochemical Concepts of the Lithium Metal Anode in Solid-State Batteries. *Chem. Rev.* **120**, 7745–7794 (2020).

14. Krauskopf, T., Hartmann, H., Zeier, W. G. & Janek, J. Toward a Fundamental Understanding of the Lithium Metal Anode in Solid-State Batteries—An Electrochemo-Mechanical Study on the Garnet-Type Solid Electrolyte $Li_{6.25}Al_{0.25}La_3Zr_2O_{12}$. *ACS Appl. Mater. Interfaces* **11**, 14463–14477 (2019).

15. Han, F., Zhu, Y., He, X., Mo, Y. & Wang, C. Electrochemical Stability of $Li_{10}GeP_2S_{12}$ and $Li_7La_3Zr_2O_{12}$ Solid Electrolytes. *Adv. Energy Mater.* **6**, 1501590 (2016).

16. Sharafi, A. *et al.* Surface Chemistry Mechanism of Ultra-Low Interfacial Resistance in the Solid-State Electrolyte $Li_7La_3Zr_2O_{12}$. *Chem. Mater.* **29**, 7961–7968 (2017).

17. Han, X. *et al.* Negating interfacial impedance in garnet-based solid-state Li metal batteries. *Nat. Mater.* **16**, 572–579 (2017).

18. David, I. N., Thompson, T., Wolfenstine, J., Allen, J. L. & Sakamoto, J. Microstructure and Li-Ion Conductivity of Hot-Pressed Cubic $Li_7La_3Zr_2O_{12}$. *J. Am. Ceram. Soc.* **98**, 1209–1214 (2015).

19. Thompson, T. *et al.* A Tale of Two Sites: On Defining the Carrier Concentration in Garnet-Based Ionic Conductors for Advanced Li Batteries. *Adv. Energy Mater.* **5**, 1500096 (2015).

20. Pesci, F. M. *et al.* Establishing Ultralow Activation Energies for Lithium Transport in Garnet Electrolytes. *ACS Appl. Mater. Interfaces* **12**, 32806–32816 (2020).

21. Yu, S. & Siegel, D. J. Grain Boundary Contributions to Li-Ion Transport in the Solid Electrolyte $Li_7La_3Zr_2O_{12}$ (LLZO). *Chem. Mater.* **29**, 9639–9647 (2017).

22. Cheng, L. *et al.* Effect of Surface Microstructure on Electrochemical Performance of Garnet Solid Electrolytes. *ACS Appl. Mater. Interfaces* **7**, 2073–2081 (2015).

23. Tenhaeff, W. E. *et al.* Resolving the Grain Boundary and Lattice Impedance of Hot-Pressed $Li_7La_3Zr_2O_{12}$ Garnet Electrolytes. *ChemElectroChem* **2**, 375–378 (2014).

24. Sakamoto, J., Rangasamy, E., Kim, H., Kim, Y. & Wolfenstine, J. Synthesis of nano-scale fast ion conducting cubic $Li_7La_3Zr_2O_{12}$. *Nanotechnology* **24**, 424005 (2013).

25. Cheng, E. J., Sharafi, A. & Sakamoto, J. Intergranular Li metal propagation through polycrystalline $Li_{6.25}Al_{0.25}La_3Zr_2O_{12}$ ceramic electrolyte. *Electrochimica Acta* **223**, 85–91 (2017).

26. Ren, Y., Shen, Y., Lin, Y. & Nan, C.-W. Direct observation of lithium dendrites inside garnet-type lithium-ion solid electrolyte. *Electrochem. Commun.* **57**, 27–30 (2015).

27. Li, G. & W. Monroe, C. Dendrite nucleation in lithium-conductive ceramics. *Phys. Chem. Chem. Phys.* **21**, 20354–20359 (2019).

28. Han, F. *et al.* High electronic conductivity as the origin of lithium dendrite formation within solid electrolytes. *Nat. Energy* **4**, 187–196 (2019).

29. Cao, D. *et al.* Lithium Dendrite in All-Solid-State Batteries: Growth Mechanisms, Suppression Strategies, and Characterizations. *Matter* **3**, 57–94 (2020).

30. Tsai, C.-L. *et al.* Li$_7$La$_3$Zr$_2$O$_{12}$ Interface Modification for Li Dendrite Prevention. *ACS Appl. Mater. Interfaces* **8**, 10617–10626 (2016).

31. Shen, F., Dixit, M. B., Xiao, X. & Hatzell, K. B. Effect of Pore Connectivity on Li Dendrite Propagation within LLZO Electrolytes Observed with Synchrotron X-ray Tomography. *ACS Energy Lett.* **3**, 1056–1061 (2018).

32. Raj, R. & Wolfenstine, J. Current limit diagrams for dendrite formation in solid-state electrolytes for Li-ion batteries. *J. Power Sources* **343**, 119–126 (2017).

33. Tian, H.-K., Liu, Z., Ji, Y., Chen, L.-Q. & Qi, Y. Interfacial Electronic Properties Dictate Li Dendrite Growth in Solid Electrolytes. *Chem. Mater.* **31**, 7351–7359 (2019).

34. Song, Y. *et al.* Revealing the Short-Circuiting Mechanism of Garnet-Based Solid-State Electrolyte. *Adv. Energy Mater.* **9**, 1900671 (2019).

35. Bernstein, N., Johannes, M. D. & Hoang, K. Origin of the Structural Phase Transition in Li$_7$La$_3$Zr$_2$O$_{12}$. *Phys. Rev. Lett.* **109**, 205702 (2012).

36. Jalem, R. *et al.* Concerted Migration Mechanism in the Li Ion Dynamics of Garnet-Type Li$_7$La$_3$Zr$_2$O$_{12}$. *Chem. Mater.* **25**, 425–430 (2013).

37. Squires, A. G., Scanlon, D. O. & Morgan, B. J. Native Defects and Their Doping Response in the Lithium Solid Electrolyte Li$_7$La$_3$Zr$_2$O$_{12}$. *Chem. Mater.* **32**, 1876–1886 (2020).

38. Tian, H.-K., Xu, B. & Qi, Y. Computational study of lithium nucleation tendency in Li$_7$La$_3$Zr$_2$O$_{12}$ (LLZO) and rational design of interlayer materials to prevent lithium dendrites. *J. Power Sources* **392**, 79–86 (2018).

39. Gao, B., Jalem, R. & Tateyama, Y. Surface-Dependent Stability of the Interface between Garnet Li$_7$La$_3$Zr$_2$O$_{12}$ and the Li Metal in the All-Solid-State Battery from First-Principles Calculations. *ACS Appl. Mater. Interfaces* **12**, 16350–16358 (2020).

40. Rajagopalan, M., Tschopp, M. A. & Solanki, K. N. Grain Boundary Segregation of Interstitial and Substitutional Impurity Atoms in Alpha-Iron. *JOM* **66**, 129–138 (2014).

41. Miara, L. J. *et al.* Effect of Rb and Ta Doping on the Ionic Conductivity and Stability of the Garnet $Li_{7+2x-y}(La_{3-x}Rb_x)(Zr_{2-y}Ta_y)O_{12}$ ($0 \leq x \leq 0.375$, $0 \leq y \leq 1$) Superionic Conductor: A First Principles Investigation. *Chem. Mater.* **25**, 3048–3055 (2013).

42. Xu, M. *et al.* Mechanisms of Li^+ transport in garnet-type cubic $Li_7La_3M_2O_{12}$ (M = Te, Nb, Zr). *Phys. Rev. B* **85**, 052301 (2012).

43. Dawson, J. A., Canepa, P., Famprikis, T., Masquelier, C. & Islam, M. S. Atomic-Scale Influence of Grain Boundaries on Li-Ion Conduction in Solid Electrolytes for All-Solid-State Batteries. *J. Am. Chem. Soc.* **140**, 362–368 (2018).

44. Kubicek, M. *et al.* Oxygen Vacancies in Fast Lithium-Ion Conducting Garnets. *Chem. Mater.* **29**, 7189–7196 (2017).

45. Moradabadi, A. & Kaghazchi, P. Defect chemistry in cubic $Li_{6.25}Al_{0.25}La_3Zr_2O_{12}$ solid electrolyte: A density functional theory study. *Solid State Ion.* **338**, 74–79 (2019).

46. Kc, S., Longo, R. C., Xiong, K. & Cho, K. Point defects in garnet-type solid electrolyte (c-$Li_7La_3Zr_2O_{12}$) for Li-ion batteries. *Solid State Ion.* **261**, 100–105 (2014).

47. Gao, B., Jalem, R. & Tateyama, Y. First-Principles Study of Microscopic Electrochemistry at the $LiCoO_2$ Cathode/$LiNbO_3$ Coating/β-Li_3PS_4 Solid Electrolyte Interfaces in an All-Solid-State Battery. *ACS Appl. Mater. Interfaces* **13**, 11765–11773 (2021).

48. Heyd, J., Scuseria, G. E. & Ernzerhof, M. Hybrid functionals based on a screened Coulomb potential. *J. Chem. Phys.* **118**, 8207–8215 (2003).

49. Krukau, A. V., Vydrov, O. A., Izmaylov, A. F. & Scuseria, G. E. Influence of the exchange screening parameter on the performance of screened hybrid functionals. *J. Chem. Phys.* **125**, 224106 (2006).

50. Ma, C. *et al.* Interfacial Stability of Li Metal–Solid Electrolyte Elucidated via in Situ Electron Microscopy. *Nano Lett.* **16**, 7030–7036 (2016).

51. Barroso-Luque, L., Tu, Q. & Ceder, G. An Analysis of Solid-State Electrodeposition-Induced Metal Plastic Flow and Predictions of Stress States in Solid Ionic Conductor Defects. *J. Electrochem. Soc.* **167**, 020534 (2020).

52. Ning, Z. *et al.* Visualizing plating-induced cracking in lithium-anode solid-electrolyte cells. *Nat. Mater.* 1–9 (2021) doi:10.1038/s41563-021-00967-8.

53. Tantratian, K., Yan, H., Ellwood, K., Harrison, E. T. & Chen, L. Unraveling the Li Penetration Mechanism in Polycrystalline Solid Electrolytes. *Adv. Energy Mater.* **n/a**, 2003417 (2021).

54. Choudhury, R., Wang, M. & Sakamoto, J. The Effects of Electric Field Distribution on the Interface Stability in Solid Electrolytes. *J. Electrochem. Soc.* **167**, 140501 (2020).

55. Kasemchainan, J. *et al.* Critical stripping current leads to dendrite formation on plating in lithium anode solid electrolyte cells. *Nat. Mater.* **18**, 1105–1111 (2019).

56. Porz, L. *et al.* Mechanism of Lithium Metal Penetration through Inorganic Solid Electrolytes. *Adv. Energy Mater.* **7**, 1701003 (2017).

57. Xie, H., Alonso, J. A., Li, Y., Fernández-Díaz, M. T. & Goodenough, J. B. Lithium Distribution in Aluminum-Free Cubic $Li_7La_3Zr_2O_{12}$. *Chem. Mater.* **23**, 3587–3589 (2011).

58. Kresse, G. & Joubert, D. From ultrasoft pseudopotentials to the projector augmented-wave method. *Phys. Rev. B* **59**, 1758–1775 (1999).

59. Blöchl, P. E. Projector augmented-wave method. *Phys. Rev. B* **50**, 17953–17979 (1994).

60. Nosé, S. A unified formulation of the constant temperature molecular dynamics methods. *J. Chem. Phys.* **81**, 511–519 (1984).

Supplementary Files

This is a list of supplementary files associated with this preprint. Click to download.

- SIGao0512.docx
- SIdoubleblined.docx